Available online at www.sciencedirect.com

ScienceDirect

Geochimica et Cosmochimica Acta 283 (2020) 40–53

Geochimica et Cosmochimica Acta

www.elsevier.com/locate/gca

An atomic force microscopy study of calcite dissolution in seawater

Sijia Dong [a,b,*], William M. Berelson [a], Jess F. Adkins [b], Nick E. Rollins [a], John D. Naviaux [b], Sahand Pirbadian [a], Mohamed Y. El-Naggar [a], H. Henry Teng [c]

[a] University of Southern California, Los Angeles, CA 90089, United States
[b] California Institute of Technology, Pasadena, CA, 91125, United States
[c] Institute of Surface Earth System Science, Tianjin University, Tianjin 300072, China

Received 8 November 2019; accepted in revised form 28 May 2020; available online 6 June 2020

Abstract

We present the first examination of calcite dissolution in seawater using Atomic Force Microscopy (AFM). We quantify step retreat velocity and etch pit density to compare dissolution in seawater to low ionic strength water, and also to compare calcite dissolution under AFM conditions to those conducted in bulk solution experiments (e.g. Subhas et al., 2015, Dong et al., 2018). Bulk dissolution rates and step retreat velocities are slower at high and mid-saturation state (Ω) values and become comparable to low ionic strength water rates at low Ω. The onset of defect-assisted etch pit formation in seawater is at $\Omega \sim 0.85$ (defined as $\Omega_{critical}$), higher than in low ionic strength water ($\Omega \sim 0.54$). There is an abrupt increase in etch pit density (from $\sim 10^6$ cm^{-2} to $\sim 10^8$ cm^{-2}) occurring when Ω falls below 0.7 in seawater, compared to $\Omega \sim 0.1$ in low ionic strength water, suggesting a transition from defect-assisted dissolution to homogeneous dissolution much closer to equilibrium in seawater. The step retreat velocity (v) does not scale linearly with undersaturation (1-Ω) across an Ω range of 0.4 to 0.9 in seawater, potentially indicating a high order correlation between kink rate and Ω for non-Kossel crystals such as calcite, or surface complexation processes during calcite dissolution in seawater.

Keywords: Calcite dissolution; Seawater; Atomic force microscopy

1. INTRODUCTION

Calcite plays a critical role in regulating geochemical cycles through dissolution and precipitation in aqueous environments due to the mineral's wide occurrence and high reactivity at earth's surface (Berner, 1981). For the past three decades, an increasing number of dissolution studies have focused on direct observation and quantification of the kinetics of dissolution on calcite surfaces using microscopic techniques such as AFM (e.g Hillner et al., 1992; Stipp et al., 1994; Dove and Platt, 1996; Liang et al., 1996; Liang and Baer, 1997; McCoy and LaFemina, 1997; Shiraki et al., 2000; Lea et al., 2001; Arvidson et al., 2003; Teng, 2004; Bisschop et al., 2006), Vertical Scanning Interferometry (VSI) (e.g. Fischer and Lüttge, 2007; Lüttge and Arvidson, 2010; Smith et al., 2013), X-ray reflectivity (Fenter et al., 2000), X-ray microscopy(Laanait et al., 2015), digital holographic microscopy (Brand et al., 2017), and 3D X-ray microtomography (Noiriel et al., 2018; Yuan et al., 2019). These direct observations have complemented interpretations of results

* Corresponding author at: Division of Geological and Planetary Sciences, Caltech. 1200 E California Blvd, 131-24, Pasadena, CA. 91125, United States.
E-mail address: dongsj@caltech.edu (S. Dong).

https://doi.org/10.1016/j.gca.2020.05.031
0016-7037/

obtained from solution-based bulk calcite dissolution studies (Plummer et al., 1978; Sjöberg and Rickard, 1984; Schott et al., 1989; Gutjahr et al., 1996; Cubillas et al., 2005; Xu et al., 2012), and are now further enhanced by model simulations of molecular-scale processes (Lüttge et al., 2013, 2019), which provide a critical linkage between nanoscale surface observations of crystal dissolution and the phenomenological results at scales of environmental importance.

Although the dissolution/precipitation reactions that help regulate atmospheric CO_2 on millennial timescales occur primarily in seawater, all previous AFM and VSI studies have been conducted in simple solutions of low ionic strength by adding chemicals into pure water. Even though the effects of electrolytes, inorganic ions and organic molecules on calcite dissolution have been studied separately to mimic seawater in contact with rock-forming minerals (e.g. Ruiz-Agudo et al., 2009; 2010; Arvidson et al., 2006; Xu and Higgins, 2011; Klasa et al., 2013; Lea et al., 2001; Vinson et al., 2007; Vinson and Lüttge, 2005; Freij et al., 2004; Kowacz and Putnis, 2008; Teng and Dove, 1997; Perry et al., 2004; Teng et al., 2006; Oelkers et al., 2011), no previous AFM experiment was ever done in seawater itself. However, the discrepancy between calcite dissolution rates in seawater environments and in simple freshwater solutions has long been noticed and has plagued marine chemists for decades. Early dissolution experiments in the ocean water column (Peterson, 1966; Berger, 1977; Honjo and Erez, 1978), and in seawater in the lab (Berner and Morse, 1974; Keir, 1980) reported calcite dissolution rates orders of magnitude lower than those measured in simple solutions (Sjöberg, 1976; Sjöberg and Rickard, 1985; Busenberg et al., 1986). Using a ^{13}C labeling technique to determine bulk dissolution rates much more precisely near equilibrium, our group has recently provided the kinetic rate law of calcite dissolution in seawater across the full under-saturation range, and has shown that calcite responds to Ω much differently in seawater than in low ionic strength water (Subhas et al., 2015; Dong et al., 2018; Naviaux et al., 2019). The complicated combination of electrolytes in seawater has a clear effect on the calcite dissolution rate over and above the thermodynamic driving force (1-Ω). However, it is still an open question, whether calcite dissolution in seawater is only the combined effect of individual ionic components, based on the relatively fixed seawater composition, or if complexation between different ionic components add complexity to the dissolution process.

This study aims to bridge the seawater and low ionic strength water dissolution studies from an experimental and microscale perspective. Comparisons of solution-based bulk dissolution rates between seawater and low ionic strength water are made, and further explained by AFM observations and quantifications of etch pit origination, densities and step velocities. The values of $\Omega_{critical}$ that define transitions between different dissolution mechanisms are identified by the enumeration of etch pit densities. Finally, the correlation of step-retreat velocity against saturation state in seawater is investigated mechanistically.

2. METHODS

2.1. Sample and solution preparation

Calcite {104} surfaces were obtained by using a razor blade to cleave a large crystal of optical-quality Iceland spar. An air burst was then applied to the cleaved fragment (approximately 5×5×0.5 mm) to remove small adhering particles. The fragment was subsequently adhered to a magnetic plate using double-sided adhesive tape.

The experimental solution was standard reference Dickson seawater, Batch 176 (https://www.nodc.noaa.gov/ocads/oceans/Dickson_CRM/batches.html) (major chemical composition is shown in Table S1), acidified to desired saturation states by adding HCl. The calcite-undersaturated seawater was kept in gas-impermeable bags with no headspace. Dissolved Inorganic Carbon (DIC) and alkalinity were measured to determine calcite saturation state (Ω, the ion concentration product over the stoichiometric solubility product). Ω was calculated from the CO2SYS program (Van Heuven et al., 2011) using K'_1, K'_2 (apparent dissociation constants of carbonic acid in seawater) reported by Mehrbach et al. (1973) and refit by Dickson and Millero (1987); K_{SO4} reported by Dickson et al. (1990); and borate to salinity ratio reported by Uppström (1974). The uncertainty of Ω was calculated based on the standard errors in DIC and alkalinity as described in Subhas et al. (2015) and averaged ±0.026. The determination of Ω is based on the DIC and alkalinity values of the fill bag solution, instead of the outflow solution during dissolution experiments; because there is not enough outflow solution for both measurements during most of our dissolution experiments which last <1.5 h.

2.2. *In situ* dissolution experiment set-up and AFM imaging

An Asylum Research Cypher ES Environmental Atomic Force Microscope was used to image the calcite dissolution process *in situ*. The fluid cell in this setup (Fig. 1) was not a closed chamber but a droplet exposed to the headspace. To maintain the solution chemistry, the headspace air composition was adjusted by adding gas that had a partial pressure of CO_2 in equilibrium with the solution. Two syringes were synchronized to simultaneously inject solutions into and withdraw from the droplet to maintain a constant volume. Alkalinity and DIC measurements of the influent and effluent solution confirmed that Ω remained constant throughout the experiment (Table S2).

Dissolution experiments were conducted at 21 °C and atmospheric pressure, and real time images were collected in either Tapping or Contact Mode as no obvious difference was observed between the two modes. Numerous commercially available AFM probes we tried corroded within 1–2 h in seawater, even for Au-coated silicon probes. As the probe corroded, the probe reflectance gradually decreased, and the intensity of the laser beam became too weak to detect. The two types of probes we used for experiments in this paper are: Arrow UHFAuD from Asylum Research (https://afmprobes.asylumresearch.com/arrow-uhfaud.html), and SNL-10 from Bruker

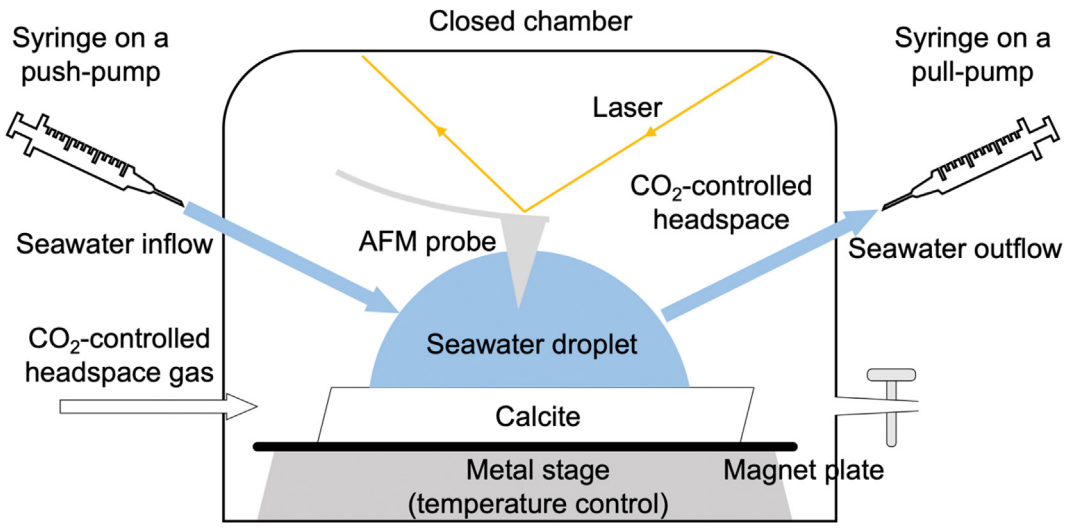

Fig. 1. AFM *in situ* dissolution experiment setup.

(https://www.brukerafmprobes.com/p-3693-snl-10.aspx). Except for the initial experiment that tested the effect of flow rate on step velocity (Fig. 2), all experiments afterwards were conducted at a flow rate of 15 mL h^{-1}; at this flow rate, water was in contact with the mineral surface for ≤1 minute (residence time).

2.3. Determination of step velocity

Due to the non-negligible drifts observed between scans in most of our experiments and the lack of a permanent local reference on the dissolving surface, we elected to use the etch pit widening rates (sum of the edge displacement perpendicular to the acute and obtuse sides) to represent the step retreat speed. The change in etch pits width is the sum of the acute $\langle \bar{4}\,4\,1\rangle_-$ and obtuse $\langle \bar{4}\,4\,1\rangle_+$ edges movement. Therefore, measured step speed is the average of the acute and obtuse step velocity. The scan rates for all experiments were either 6.5 Hz or 9.8 Hz, equivalent to 0.2–1.5 μm s^{-1} at the scan sizes used for image collection. This scan rate was significantly faster than the step retreat rates measured in all experiments (0.003–0.4 nm s^{-1}), and therefore should have a negligible influence in generating step velocity error. In addition, all step velocity calculations were made with images of the same scan direction during an experiment (either frame-up or frame-down). Because parallel edges in individual etch pits have opposite polarity ($\langle \bar{4}\,4\,1\rangle_-$ and $\langle \bar{4}\,4\,1\rangle_+$), the pit widening rate was therefore the average of the acute and obtuse step retreat velocities. Separate measurements for the acute and obtuse velocities were only made in two dissolution experiments (when image drifting was insignificant) to approximately estimate the ratio of the acute to obtuse velocity during calcite dissolution in seawater.

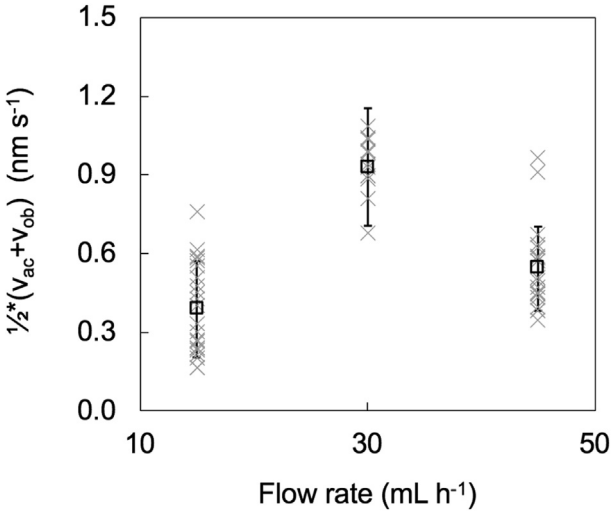

Fig. 2. Average step velocity of acute and obtuse edges at three different flow rates (15 mL h^{-1}, 30 mL h^{-1}, 45 mL h^{-1}) at $\Omega = 0.37 \pm 0.01$. The grey crosses are velocities at different individual etch pits. The squares are the mean values of the crosses, with the error bars representing one standard deviation of the population.

When measuring the step velocities, images were rotated so that the step edges we used to measure pit widths are vertical, and the measurements of pit widths were parallel to the edge motion (Fig. 3). Pit widths were only measured at etch pits that have all four edges (indicated by yellow arrows in Fig. 3). We excluded etch pits that had coalesced with other etch pits or long steps (indicated by black arrows in Fig. 3).

Uncertainty in our measured step velocities was determined as the standard error of a population of step velocities at 1 to 8 different etch pits and at 2 to 6 different time periods for each of our 7 experiments (Table 1). Measured step velocity was found to be independent of time and location (Fig. S1), and the variation was largely due to the limited precision in width measurement within the image analysis program Gwyddion. Specifically, the precision of the distance measurement was ±10 nm, whereas step velocities (average of acute and obtuse velocities) in our

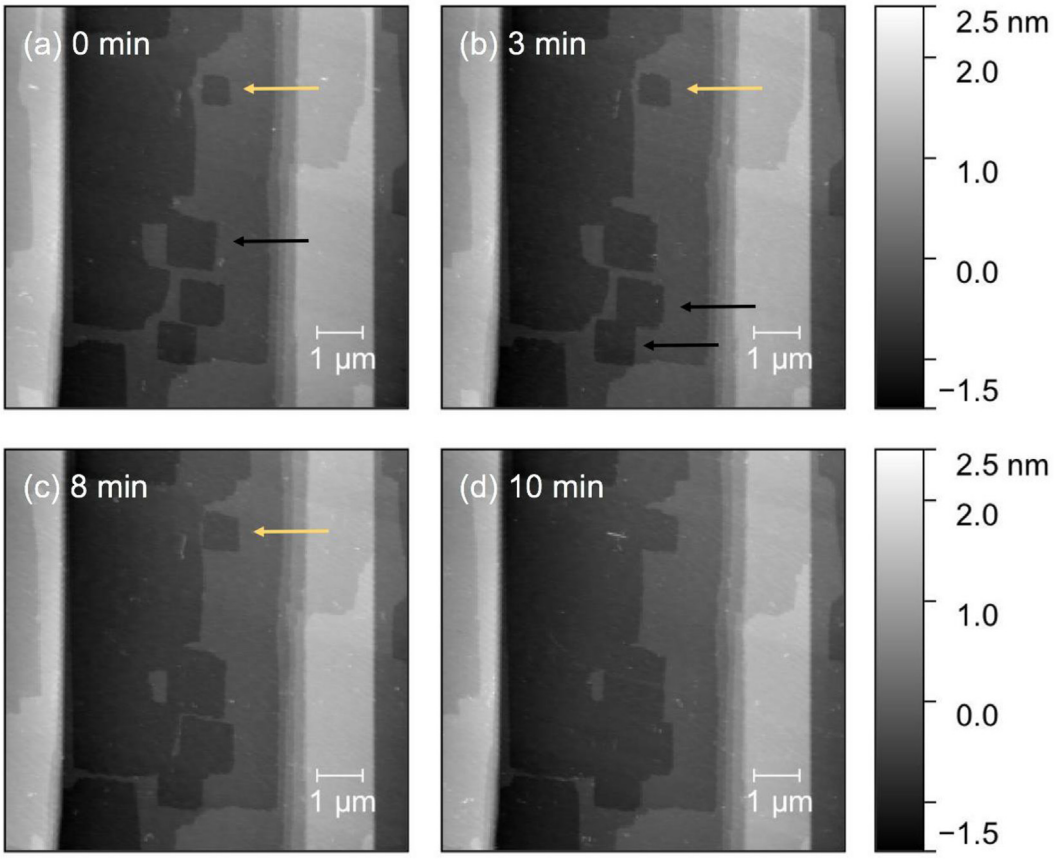

Fig. 3. One example of dissolution on the calcite {104} cleavage surface in seawater ($\Omega = 0.46 \pm 0.01$). 0 min in Fig. 3a is actually 37 min after the start of the continuous seawater flow.

Table 1
Average of acute and obtuse step velocities against saturation states.

Expt. No.	DIC (μmol kg^{-1})	Alkalinity (μmol kg^{-1})	Ω	No. of v in the population statistics	$\frac{1}{2} * (v_{ac} + v_{ob})$(nm s^{-1})
AF-3	2025.0 ± 3.5	1922.9 ± 0.9	0.46 ± 0.01	16	0.219 ± 0.031
AF-5	2027.8 ± 0.9	1960.3 ± 0.6	0.58 ± 0.01	9	0.0577 ± 0.0086
AF-7	2024.8 ± 10.1	1984.4 ± 0.4	0.72 ± 0.03	7	0.0140 ± 0.0031
AF-9	2021.3 ± 5.8	1997.2 ± 2.5	0.82 ± 0.04	2	0.0137 ± 0.0055
AF-18	2015.1 ± 2.1	1942.4 ± 1.9	0.56 ± 0.01	10	0.0143 ± 0.0025
AF-20	2064.3 ± 6.4	1926.3 ± 2.8	0.37 ± 0.01	22	0.388 ± 0.037
AF-8	2021.3 ± 5.8	1997.2 ± 2.5	0.87 ± 0.04	3	0.00298 ± 0.00019

experiments were 0.003–0.4 nm s^{-1} (e.g., every 15 min, the changes in width were 5–700 nm). Due to the rapid probe corrosion in the experimental seawater, generally experiments lasted less than 1 h. Therefore, for determinations of widths within several minutes, especially in slow dissolution experiments, large errors exist because the changes in width are comparable to the precision of our measurement.

3. RESULTS

3.1. Effect of flow rate on dissolution and the variation of step velocity on the calcite surface

For etch pits that are one monolayer deep, average step velocities of acute and obtuse edges vary by as much as 6 times between different etch pits during a single dissolution experiment at $\Omega = 0.37 \pm 0.01$ (Fig. 3). Such variability can only be accounted for by taking many different measurements. The mean values of average step velocities of the top monolayer at fluid flow rates of 15 mL h^{-1}, 30 mL h^{-1}, 45 mL h^{-1} are within one standard deviation of each other, indicating that dissolution is not limited by diffusion for single monolayers above 15 mL h^{-1}. Because $\Omega = 0.37 \pm 0.01$ is the lowest saturation state among all dissolution experiments in this study, and step velocity at this saturation is the highest, this experiment would be most sensitive to the impact of our cell and flow design. Since it shows no significant difference in step velocity at the three flow rates, we conclude that all dissolution experiments conducted with flow rates = 15 mL h^{-1} can be considered

surface-controlled instead of diffusion-controlled. Calculated Ω values for the inflow and the outflow solutions, based on DIC and alkalinity measurements, are similar within error (Table S2).

3.2. Etch pit morphology in seawater and etch pit density vs. undersaturation

Etch pits in seawater are rhombic with no significant corner rounding observed during dissolution (Fig. 3). Dissolution experiments at $\Omega = 0.88 \pm 0.04$ and 0.87 ± 0.04 show no etch pit formation for 30 min within the total scanned area of 17.04 μm × 17.04 μm, and dissolution only occurs as step retreat of existing edges (Fig. 4a). The highest Ω at which etch pit formation is observed is 0.82 ± 0.04 (1 etch pit in 31.9 μm^2 throughout 60 min). Below $\Omega = 0.82 \pm 0.04$, dissolution proceeds in the form of both step retreat and surface pitting (Fig. 4b). Etch pit density increases significantly below $\Omega \sim 0.7$, and the rise is used to distinguish the homogeneous etch pit mechanism from the defect-assisted etch pit mechanism, which will be discussed further in Section 4.2.

3.3. The dependence of step velocity and dissolution rate on saturation state

Despite the scatter of data points, average step velocity increases as Ω decreases (Fig. 5, Table 1), with an apparent reaction order n = 2.6. The scatter results from the variation of step velocities between different etch pits and time periods (Fig. 2 and Fig. S1), and is also potentially due to the limited precision in etch pit width measurement (see as discussed in Section 2.3).

The ratio of obtuse and acute step velocities is determined at $\Omega = 0.46$ and $\Omega = 0.37$, during which experiments no obvious image drift was observed. At two different etch pits in the experiment at $\Omega = 0.46$, $v_{ob}/v_{ac} = 9$ and 5.6, respectively. At $\Omega = 0.37$, for the continuous spreading of an etch pit, average step velocities at 4 different time intervals give $v_{ob}/v_{ac} = 9.6$. Therefore, our study suggests that calcite dissolution in natural seawater has a v_{ob}/v_{ac} of roughly 5 to 10. A more accurate determination of v_{ob}/v_{ac} will require a fixed reference mark on the dissolving surface such as a manually-placed inert feature.

4. DISCUSSION

4.1. Comparison of low ionic strength water studies and seawater

Even though the effects of different electrolytes, inorganic ions and organic molecules on calcite dissolution have been widely studied to mimic the reaction in natural aqueous systems such as seawater, all previous AFM and VSI studies were conducted by adding components to deionized water, forming low ionic strength water. In order to investigate the particular effects of individual ions, each component was added separately. Seawater, however, has a combination of assorted ions and the interaction among these species may lead to potentially distinct dissolution phenomena. We summarize some published effects that these components have on calcite dissolution, and discuss

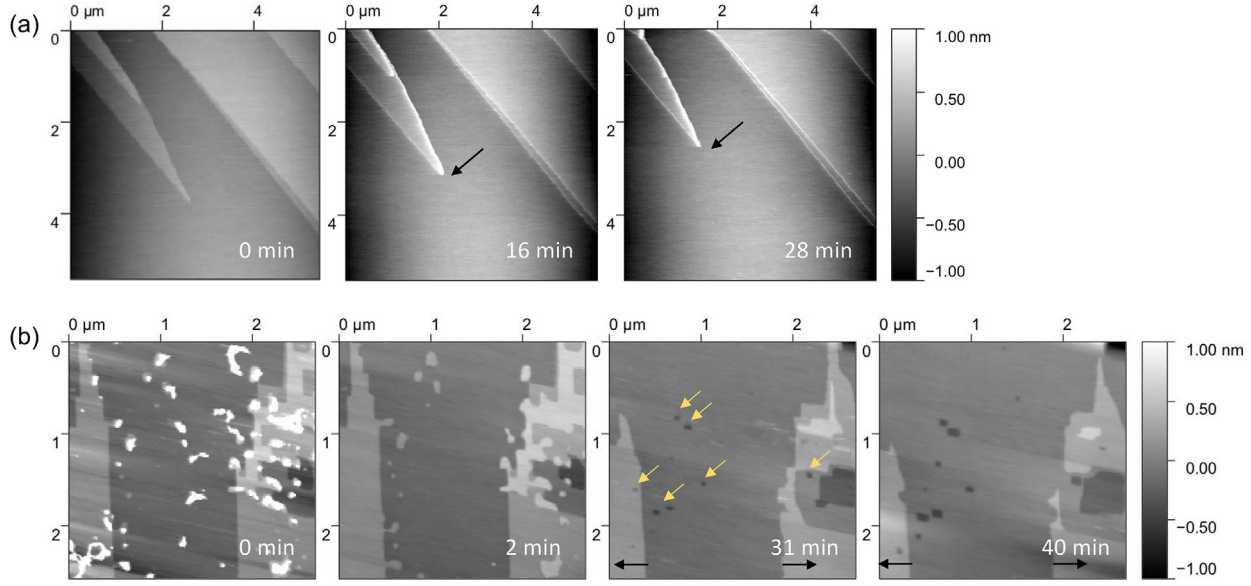

Fig. 4. (a) $\Omega = 0.88 \pm 0.04$; (b) $\Omega = 0.50 \pm 0.02$ (etch pits formed before t = 31 min, but image quality was poor). At $\Omega = 0.88 \pm 0.04$, dissolution only happens as step retreat (black arrows). No etch pit formation was found for 30 min within the total scanned area of 17.04μm × 17.04 μm. At $\Omega = 0.50 \pm 0.02$, dissolution happens both at existing step edges (black arrows) and at newly-formed etch pits (yellow arrows). The highest Ω observed for etch pit formation is 0.82 ± 0.04 with a pit density of 3.1×10^6 cm^{-2}. (For interpretation of the references to colour in this figure legend, the reader is referred to the web version of this article.)

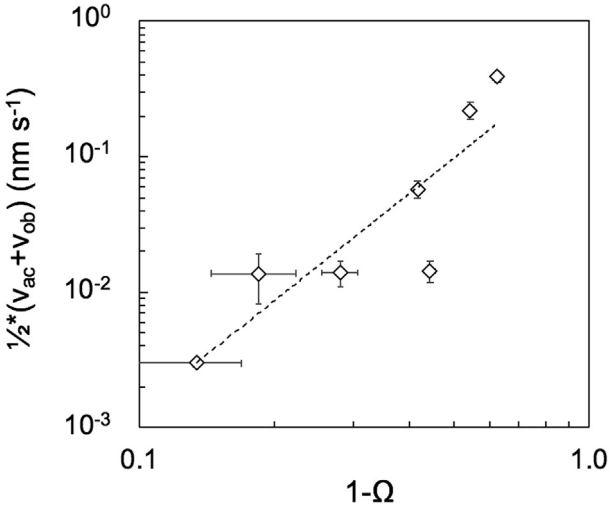

Fig. 5. Average step velocity of acute and obtuse edges vs. undersaturation. Note that this is a log–log plot, so the slope of 2.6 indicates that the correlation is a power function with an order of 2.6.

whether the concentrations in seawater are comparable to the concentrations needed to affect dissolution behaviors (Table 2).

Based on the low ionic strength water studies, various ions and organic matter can affect calcite dissolution by altering etch pit morphology, density, spreading and deepening rate. Etch pit morphology may be altered if acute and obtuse steps are affected differently. Specifically, several studies have reported rounded etch pits with the addition of CO_3^{2-}, PO_4^{3-}, Mn^{2+} and Mg^{2+} (Lea et al., 2001; Vinson et al., 2007; Klasa et al., 2013; Arvidson et al., 2006; Ruiz-Agudo et al., 2009; Xu and Higgins, 2011). While the concentrations of CO_3^{2-}, PO_4^{3-}, and Mn^{2+} in seawater are below the reported values necessary to alter etch pits morphology modification (Table 2), the concentration of Mg^{2+} in seawater is ~0.05 mol kg^{-1}, higher than the reported [Mg^{2+}] that affects etch pit morphology in Arvidson et al. (2006) (8×10^{-4} mol kg^{-1}), albeit lower than the concentration in Ruiz-Agudo et al. (2009) (1 mol kg^{-1}). Nevertheless, our results of calcite etch pit morphology in seawater show no obvious difference than previously published freshwater morphology (Fig. 3).

In addition to etch pit morphology, Mg^{2+}, SO_4^{2-} and PO_4^{3-} are also suggested to increase the density of etch pits nucleated on calcite surfaces (Ruiz-Agudo et al., 2009; Klasa et al., 2013). Meanwhile, CO_3^{2-}, Mn^{2+}, Sr^{2+}, NH_4^+, Mg^{2+}, and SO_4^{2-} are supposed to decrease step velocities during calcite dissolution (Lea et al., 2001; Klasa et al., 2013; Ruiz-Agudo et al., 2009). However, only [Mg^{2+}] and [Sr^{2+}] in seawater are higher than the concentrations required for the effects as reported in the literature, and the effect of Sr^{2+} on step velocity is small (Lea et al., 2001) (comparable to the error bars) (Table 2). Therefore, the combination of the ions in seawater, especially Mg^{2+}, may have a dual and opposing effect on calcite dissolution – the promotion of etch pit nucleation and the inhibition of etch pit spreading velocity. The comparison of etch pit density and step velocity between calcite dissolution in low ionic strength water and seawater will be discussed in detail in the following sections.

4.2. Etch pit density and the identification of changes in dissolution mechanisms

Solution-based bulk dissolution rates (Fig. 6a) show different dependencies on saturation state in low ionic strength water and seawater. These separate behaviors are likely the combined effect of the different responses of etch pit density (Fig. 6b) and step velocity (Fig. 6c) to the solution saturation state. Near equilibrium, solution-based rates in seawater are lower than in low ionic strength water by 2–4 orders of magnitude. But the two rates become comparable at $\Omega < 0.6$ (Fig. 6a). In this section, AFM-determined etch pit density is used to identify which dissolution mechanisms dominate across a wide range of Ω values and to compare the $\Omega_{critical}$s at which the mechanism changes between seawater and low ionic strength water (Fig. 6b).

Table 2
Published effects of different ions on calcite dissolution and the ion concentrations in Dickson standard seawater.

Ion	Effect(s) on dissolution	Minimum concentration for the effect(s) (mol kg^{-1})	Concentration in Dickson standard seawater (mol kg^{-1})	Reference
CO_3^{2-}	Etch pit morphology, step velocity	1.5×10^{-4} (*)	$2–6\times10^{-5}$	Lea et al. (2001)
PO_4^{3-}	Etch pit morphology and density, step velocity	10^{-3}	2.9×10^{-7}	Klasa et al. (2013)
Mn^{2+}	Etch pit morphology, step velocity	1.0×10^{-6}	3.6×10^{-10}	Lea et al. (2001); Vinson et al., 2007
Mg^{2+}	Etch pit morphology, density, and depth, step velocity	10^{-5}–10^{-3}	5×10^{-2}	Arvidson et al. (2006); Ruiz-Agudo et al. (2009); Xu and Higgins (2011)
SO_4^{2-}	Etch pit density, depth, step velocity	10^{-1}	3×10^{-2}	Ruiz-Agudo et al. (2009)
Sr^{2+}	Step velocity (slightly)	5×10^{-6}	9×10^{-5}	Lea et al. (2001)

* Indicates that the concentration is the minimum addition in the study.

Table 3
A comparison of bulk rate and step velocity between this study and previous publications.

Log bulk rate (mol cm^{-2} s^{-1})	Step velocity (nm/s)	$(v_o + v_a)/2$ (nm/s)	Material	Solution	$\Omega_{calcite}$	pH	T (°C)	Method	Reference
−14.1 to −11.9	N.A.	0.003–0.4	Iceland Spar (104) surface	Natural seawater	0.4–0.9	7.0–7.3	21	AFM	This study
−14.5 to −9.9	N.A.	N.A.	Calcite powder	Natural seawater	0.02–0.99	5.9–7.3	21	Bulk dissolution	Subhas et al. (2017)
−13.0 to −10.4	N.A.	N.A.	Iceland Spar	NaCl-$NaHCO_3$-$CaCl_2$ solution	0.1–0.8	8.0–8.1	20	VSI and bulk dissolution	Smith et al. (2013)
−12.0 to −10.2	N.A.	N.A.	Fragmental and powder samples	$NaHCO_3$-$CaCl_2$ solution	$10^{-4} \sim 0.9$	>8	25	Bulk dissolution	Xu et al. (2012)
−9.8	N.A.	N.A.	Calcite powder	HCl solution	10^{-3}	7.3	25	Bulk dissolution	Cubillas et al. (2005)
N.A.	v_o = 0–3; v_a = 0–0.6	0–1.7	Iceland Spar (104) surface	NaCl-$NaHCO_3$-$CaCl_2$ solution	0.09–1.2	7.8–8.3	50	AFM	Xu et al. (2010)
−9.5	v_o = 3; v_a = 1	2	Iceland Spar (104) surface	NaCl solution	10^{-7}	7.6	21	AFM	Shiraki et al. (2000)
N.A.	v_o = 0.90; v_a = 0.67	0.79	Iceland Spar (104) surface	Na_2CO_3 solution	0.07	8.9	22	AFM	Lea et al. (2001)
−10.6	v_o = 4.2; v_a = 0.9	2.6	Iceland Spar (104) surface	HCl solution	$10^{-2.15}$	7.5	22	AFM	De Giudici (2002)
−11.0	0.00337	0.00337	Iceland Spar (104) surface	$NaHCO_3$-Na_2CO_3 solution	$10^{-3.41}$	8.8	25	VSI	Arvidson et al. (2003)
−11.6	v_o = 0.04; v_a = 0.74	0.39	Iceland Spar (104) surface	$NaHCO_3$ solution	$10^{-3.39}$	8.8	25	VSI, AFM	Arvidson et al. (2006)
−11.2	v_o = 0.27; v_a = 1.14	0.71	Iceland Spar (104) surface	Na_2CO_3 solution	$10^{-3.59}$	8.7	22	VSI, AFM	Vinson and Lüttge (2005)
−10.6	v_o = 1.98; v_a = 1.51	1.75		NaCl solution	N.A.	8.6			
N.A.	v_o = 0.29–2.10; v_a = 0.19–0.55	0.24–1.3	Iceland Spar (104) surface	Milli-Q water	N.A.	5.6–8.3	30	AFM	Harstad and Stipp (2007)

* Except for this study and Subhas et al. (2017), all other studies in Table 3 are considered as low ionic strength water studies (Milli-Q water w/wo addition of certain ions).

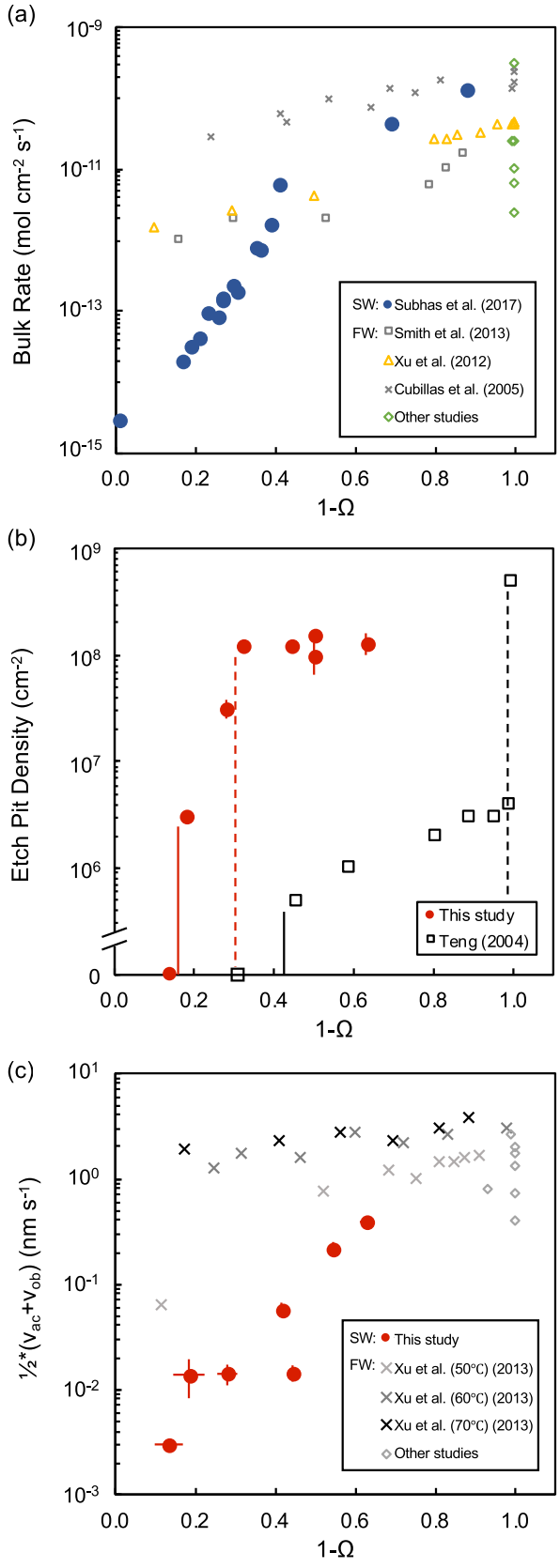

Distinct dissolution mechanisms at different saturation states in low ionic water have been both theoretically proposed and experimentally identified (Holdren and Berner, 1979; Brantley et al., 1986; Gratz et al., 1991; Stipp et al., 1994; Lasaga and Lüttge, 2001; Teng, 2004; Dove et al., 2005; Arvidson and Lüttge, 2010). Proceeding from near-equilibrium to farther from equilibrium, dissolution occurs as (1) retreat of pre-existing steps at edges, corners and dislocations; (2) opening of etch pits at defects; and finally (3) opening of etch pits homogenously across the mineral surface. After formation, etch pits can either spread as "2D pancakes" (Dove et al, 2005), or "step-waves" that contain multiple layers (Lasaga and Lüttge, 2001). The transitions between different dissolution mechanisms happen at $\Omega_{critical}$, and imply a discontinuous relationship between rate and undersaturation.

The determination of $\Omega_{critical}$ in bulk dissolution experiments (Subhas et al., 2017; Dong et al., 2018; Naviaux et al., 2019) is done by fitting dissolution rates to a mechanistic model (Dove et al, 2005) and identifying the breaks in slope in a plot of rate vs. undersaturation. We set out to determine if these transitions in mechanism can be verified by AFM observations. Assuming the onset of the defect-assisted etch pit mechanism is marked by the highest Ω observed for etch pit formation, and the onset of the homogeneous etch pit mechanism is revealed by a precipitous increase of pit density as Ω falls below a critical value, Teng (2004) measured pit densities against solution undersaturation in weak electrolyte solutions. This work showed an increase of pit densities as Ω falls, and a very rapid rise at $\Omega = 0.007$, as pit density increases from 4×10^{6} cm^{-2} to 5×10^{8} cm^{-2} (Teng, 2004). Compared to the observations in weak electrolyte solutions, we have previously reported $\Omega_{critical}$ for the opening of defect-assisted etch pits in seawater is $\Omega = 0.9$ (versus $\Omega = 0.54$ in low ionic strength water), and the $\Omega_{critical}$ for homogeneous etch pit formation at $\Omega = 0.75$ (versus $\Omega = 0.007$ in low ionic strength water) in bulk dissolution experiments (Naviaux et al., 2019).

Fig. 6. Comparisons of (a) bulk dissolution rate, (b) etch pit density and (c) step velocity between dissolution in seawater (SW) and in low ionic strength water (FW for freshwater). In 6b, the solid and dashed lines represent the transitions of the dominating surface dissolution mechanism, for seawater (red) and low ionic water (black) respectively. Solid lines are the $\Omega_{critical}$ between step retreat and defect-assisted etch pit formation. Dashed lines are the $\Omega_{critical}$ between defect-assisted and homogeneous etch pit formation. Subhas et al. (2017) and this study are in seawater, all others are in low ionic strength water. "Other studies" in Fig. 6a and 6c include: Shiraki et al., 2000; De Giudici, 2002; Arvidson et al., 2003; Arvidson et al., 2006; Vinson and Lüttge, 2005; Lea et al, 2001; Harstad and Stipp, 2007. Except for Xu et al. (2010) which has experimental temperatures of 50–70 °C, all other studies are between 20 °C and 25 °C. Experimental details are listed in Tables 1, 3 and 4.

Table 4
Measured etch pit density against solution undersaturation.

Expt. No.	DIC (μmol kg^{-1})	Alkalinity (μmol kg^{-1})	Ω	Average etch pit numbers	Error etch pit numbers	Image area (μm^2)	Average etch pit density (cm^{-2})	Error etch pit density (cm^{-2})
AF-9	2021.3 ± 5.8	1997.2 ± 2.5	0.82 ± 0.04	1	0	31.9	3.1×10^6	0
AF-14	2023.1 ± 10.1	1982.5 ± 1.7	0.72 ± 0.05	10	2	31.6	3.2×10^7	6.3×10^6
AF-17	2010.4 ± 9.6	1964.3 ± 0.3	0.68 ± 0.05	17	2	13.9	1.2×10^8	1.4×10^7
AF-18	2015.1 ± 2.1	1942.4 ± 1.9	0.56 ± 0.01	8	0	6.4	1.2×10^8	0
AF-11	2030 ± 10	1940 ± 2	0.50 ± 0.05	9	3	9.2	9.8×10^7	3.3×10^7
AF-12	2032.9 ± 4.3	1942.5 ± 2.2	0.50 ± 0.02	23	3	14.7	1.5×10^8	1.7×10^7
AF-20	2064.3 ± 6.4	1926.3 ± 2.8	0.37 ± 0.01	33	8	25.0	1.3×10^8	3.0×10^7
Teng (2004)	N.A.	N.A.	0.012–0.54	N.A.	N.A.	N.A.	$<4\times10^6$	N.A.
	N.A.	N.A.	0.007	N.A.	N.A.	N.A.	5×10^8	N.A.

* Error in etch pit numbers is determined by the variation between images at different time.

The AFM measurements generally support our earlier reported $\Omega_{critical}$ values in seawater. No etch pits are observed during dissolution experiments at $\Omega = 0.87$ and 0.88; dissolution only occurs as step retreat (Fig. 4a). The highest Ω observed for etch pit formation is 0.82, with a pit density of 3.1×10^6 cm^{-2} (Fig. 6b, Table 4). The transition between step retreat and defect-assisted etch pit mechanisms is therefore between 0.82 and 0.87 (red solid line in Fig. 6c), comparable to $\Omega_{critical} = 0.87$ in Dong et al. (2018) and 0.9 in Naviaux et al. (2019). Below $\Omega = 0.7$, pit density increases abruptly to $\sim10^8$ cm^{-2} (Fig. 6c), similar to the pit density reported for homogeneous etch pit formation mechanism far from equilibrium in Teng (2004) ($n_s = 10^8$ sites cm^{-2}) and in Ruiz-Agudo et al. (2009) ($n_s = 10^9$ sites cm^{-2}). The significant difference in etch pit density above and below $\Omega = 0.7$ (red dashed line in Fig. 6c) in seawater indicates the onset of the homogeneous etch pit formation mechanism, which also agrees with the corresponding $\Omega_{critical} = 0.75$ proposed by Naviaux et al. (2019). The fact that the onsets of both defect-assisted and homogeneous etch pit mechanisms occur at higher Ω in seawater (red solid and dashed lines in Fig. 6c) than in low ionic strength water (black solid and dashed lines in Fig. 6c) is demonstrated in both solution-based experiments and this AFM work. This basic result implies that the surface energy of calcite is lower in seawater than it is in low ionic strength water. Based on the slopes of our bulk dissolution rate data in the 2D etch pit mode, we diagnosed a surface energy of ~34 mJ m^{-2} (Naviaux et al., 2019), while the reported freshwater value is almost three times higher at 97 mJ m^{-2} (Lasaga, 1998; Steefel and Van Cappellen, 1990).

The offset in $\Omega_{critical}$ between seawater and low ionic strength solutions, and the implication of surface energy lowering, could be related to the effects of other ions besides Ca^{2+} and CO_3^{2-} (e.g. Mg^{2+}, SO_4^{2-} etc.) on etch pit density. Although the effects of these ions have yet to be carefully tested in seawater near equilibrium, AFM studies and molecular dynamics simulations in simple solutions suggest several potential mechanisms. Mg^{2+} has been reported to increase the density and depth of etch pits nucleated on calcite surfaces at concentrations above 0.05 mol kg^{-1} far from equilibrium (Ruiz-Agudo et al., 2009). A molecular dynamics (MD) simulation by Kerisit and Parker (2004) has shown that Mg^{2+} is able to attract water molecules from the calcite surface to retain a full coordination shell (i.e. 6 water molecules) once it adsorbs as an inner-sphere complex directly above a surface carbonate group. As a result, water molecules could be transferred from surface calcium sites on calcite during magnesium adsorption. Such a strong magnesium-surface interaction and the fact that magnesium can disrupt the surface hydration layer can lead to surface destabilization, and ultimately favor nucleation of etch pits. A reduction in the kinetic barrier associated with the magnesium-calcite surface interaction initiates etch pit nucleation which manifests itself as an increase in etch pit density.

In addition to Mg^{2+}, SO_4^{2-} has also been reported to increase the etch pit deepening rate and etch pit density during calcite dissolution in simple ionic solutions (Ruiz-Agudo et al., 2009). One possible explanation of the SO_4^{2-} effect is via an increase in Mg-adsorption on carbonates. Specifically, the rate limiting step for Mg^{2+} adsorption onto carbonates is its dehydration (Lippmann, 1973), and SO_4^{2-} is known to enhance cation desolvation through the formation of ion pairs (Piana et al., 2006). As a result, Mg^{2+} and SO_4^{2-} hydrated ions in the solution combine to form double solvent separated ion pairs or contact ion pairs (Rudolph et al., 2004), and water molecules are lost from such complexes. Dehydrated Mg^{2+} ions are then available to adsorb on carbonates. In this respect, Brady et al. (1996) have also shown that adsorption of magnesium on carbonates is enhanced in sulfate-rich solutions during dolomite growth. These previous studies suggest a potential SO_4^{2-} effect on etch pit formation during calcite dissolution. However, these mechanisms are based upon studies conducted in simpler ionic solutions than seawater and at Ω values far from equilibrium. An important next step is to investigate how the two negatively charged species, SO_4^{2-} and CO_3^{2-}, might compete for surface complexation sites on calcite in seawater, and how this competition might be affected by the presence of Mg^{2+}.

4.3. Dependence of step velocity on the saturation state

Solution-based bulk mineral dissolution rate and step velocity show similar patterns in how they differ between

seawater and low ionic strength water, with rates being lower in seawater near equilibrium but similar far from equilibrium (Fig. 6a and 6c). For the comparison of step velocity, however, it is worth noting that most freshwater studies were conducted at extremely low saturation states, and the only study conducted at high Ω was aimed at conditions of geological carbon sequestration, and thus had high temperature (Xu et al., 2010). These authors showed that step velocities are smaller at lower temperature. However, because there is only one data point at 50 °C between Ω = 0.5 and 1 in Xu et al. (2010), it is difficult to extrapolate the high temperature velocities to 21 °C at near equilibrium conditions.

In surface nucleation and spiral growth models, the speed of a moving step, v, is related to the kinetic coefficient β and the solution saturation state Ω via (Chernov, 1984; Malkin et al., 1989):

$$v = \omega\beta C_e(1-\Omega) \quad (1)$$

where ω is the molecular volume of a molecule in the crystal (6.12×10^{-29} m^3 $molecule^{-1}$), and C_e is the mineral solubility (2.59×10^{22} atoms m^{-3}). The same mechanistic model has been suggested to work for quartz dissolution by analogous processes (Dove et al., 2005). For dissolution, the kinetic coefficient β depends on temperature and the activation energy of detachment from steps (ϵ_{step}) during step retreat:

$$\beta = \beta_0 \exp\left(-\frac{\epsilon_{step}}{k_b T}\right) \quad (2)$$

where k_b is Boltzmann's constant, T is temperature (Kelvin). At pre-existing steps or after an etch pit is initiated, dissolution occurs as the step retreats and therefore β should remain constant during dissolution. As a result, v (measurable on AFM) will be a linear function of Ω at a given temperature. However, these models were developed for Kossel crystals or for AB crystals where the anion and the cation exist in solution in their solid stoichiometric ratio. Here we address whether calcite dissolution in seawater still has a liner dependence of step velocity on Ω, that is to say a constant kinetic coefficient, β.

Previous calcite dissolution experiments in low ionic strength solutions showed a generally linear dependence of step velocity on saturation state below Ω = 0.8, but the linear trend fell off near equilibrium (Xu et al., 2010). In addition, our group has consistently reported a highly nonlinear dependence of bulk dissolution rate on saturation state in seawater (Subhas et al., 2015; Dong et al., 2018; Naviaux et al., 2019). Because it is still an open question whether Eq.1 applies, we use β^* to describe the measured quantity, v / $\{\omega C_e(1-\Omega)\}$.

In our group's previous study, where we used the mechanistic framework in Dove et al. (2005) to identify transitions of dissolution mechanisms based on bulk rate measurements (Naviaux et al., 2019), we assumed a constant β^* across Ω values within the homogeneous etch pit spreading mechanism and the defect-assisted etch pit mechanism, and that there was a different β^* for the step retreat mechanism. Under the assumption that Eq. (1) held true, Naviaux et al. were able to fit their bulk dissolution data from $0 < \Omega < 0.9$ (defect-assisted and homogenous etch pit formation) using a $\beta^* = 5\times10^{-3}$ m s^{-1}, and from $0.9 < \Omega < 1$ (step propagation) with a much smaller value of $\beta^* = 3\times10^{-7}$ m s^{-1}. The authors noted that, when extrapolating to Ω = 0, the β^* of 5×10^{-3} m s^{-1} implied a relatively fast upper limit of v of ~10 nm s^{-1} at 21 °C in seawater.

Direct measurements of step velocities using AFM allow us to calculate the "kinetic coefficient" without making assumptions about the etch pit density (n_s) and the independence of β^* on Ω within the same dissolution mechanism, as was done for Naviaux et al. (2019). AFM-determined step velocities in this work are not linear with saturation states (Fig. 5, slope > 1 in the log–log plot). Upon measuring the mean step velocity of acute and obtuse steps, the mean "kinetic coefficient" for the two types of edges can be calculated at different saturation states. Note that because we use etch pit widening rates to calculate step velocity, the β^*s we obtain are only between $0 < \Omega < 0.9$, for homogenous 2D dissolution and defect-assisted dissolution. Our results show a variable β^* across an Ω range of 0.4 to 0.9 in seawater, with significantly higher values at lower Ω (Fig. 7). From near equilibrium to Ω = 0.4, β^* increases from 1.4×10^{-5} m s^{-1} to 3.9×10^{-4} m s^{-1}. An extrapolation to Ω = 0 suggests an upper limit for average acute and obtuse step velocity of ~1 nm s^{-1} (Fig. 5), an order of magnitude lower than the value derived from bulk rate measurements in Naviaux et al. (2019). This offset between observed and calculated values shows that the surface nucleation/dissolution models (i.e., Chernov, 1984; Malkin et al., 1989; Dove et al, 2005) may be incomplete for calcite dissolution in seawater.

One possible reason that may account for the nonlinear dependence of step velocity on Ω for calcite dissolution in seawater is that the linear relationship is derived using a Kossel crystal model (Kossel, 1927; Stranski, 1928) containing only one type of growth unit (e.g. quartz SiO_2 in Dove

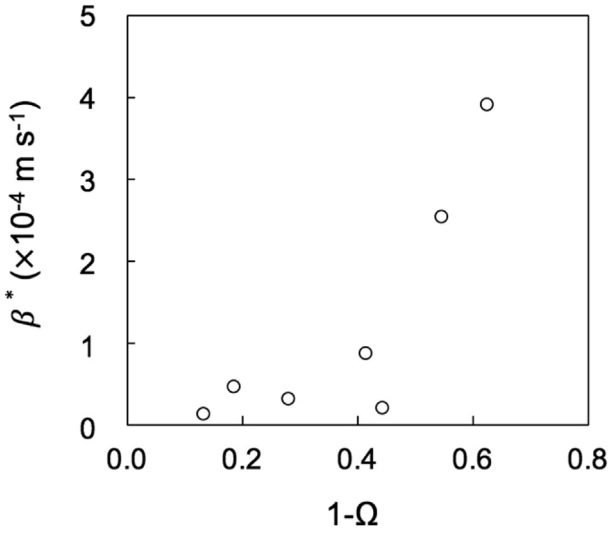

Fig. 7. Our measured "kinetic coefficient" β^* as a function of (1-Ω).

et al., 2005), whereas calcite is a non-Kossel crystal and seawater has a variable and large ratio of Ca:CO_3. The derivation of the linear relationship links the step velocity (v) to the motion of a single kink along the step (v_k), which is further related to the difference between the rates of attachment (j^+) and detachment (j^-) of the growth unit (Qiu and Orme, 2008). The attachment and detachment rates are directly related to the chemical potentials of the starting and activated states, and therefore kink mobility ($j^{\pm}$) is a linear function of Ω. In the limit of infinitely long steps with growth occurring via attachment and detachment at kink sites, and under the further assumption that nucleation of kink sites is not rate limiting, v can be related to the v_k by

$$v = b_{\perp} * \rho_k * v_k \quad (3)$$

where $b_{\perp}$ is the molecular distance in the direction of the step motion (or perpendicular to the step edge) and ρ_k is the kink density. When kink-nucleation and supersaturation dependent effects are negligible compared to kinks produced by thermal fluctuations, the kink density may be expressed as a constant (Chernov, 2004; Chernov et al., 2004). This assumption leads to the common expression of a linear dependence of step velocity on saturation state (Eq. (1)) for a Kossel crystal model.

However, for non-Kossel crystals, there are different $j^{\pm}$s when growth/dissolution requires incorporation/detachment of alternating ions (e.g. Ca^{2+} and CO_3^{2-} for calcite). As a result of a cooperative interaction of different ions within the unit cell, the linear dependence of the kink velocity (v_k) on the saturation state will no longer hold true (Chernov, 2004; Zhang and Nancollas, 1998; Qiu and Orme 2008; Nehrke et al., 2007; Stack and Grantham, 2010; Wolthers et al., 2012; Nielsen et al., 2012). For calcite dissolution, specifically, mechanistic models suggest different site-specific reactions with different rate constants at the $>CO_3^-$ and $>Ca^+$ sites of the calcite surface (Arakaki and Mucci, 1995), which also imply different $j^{\pm}$s at the kink sites. This proposed mechanism in low ionic strength water will be altered by the complexation of surface sites from the major ions present in seawater (Ding and Rahman, 2018; Song et al., 2017).

In addition to different $j^{\pm}$s for non-Kossel crystal, another reason that may cause the non-linearity in the step velocity vs. Ω is the change of chemical potential due to the surface complexation processes between calcite and the ions in seawater. This statement is supported by the fact that the linearity between step velocity vs. Ω is higher in low ionic strength water (Xu et al., 2010) than in seawater (this study). In addition, the surface nucleation/dissolution models also do not permit an analysis of how solution stoichiometry may affect crystal growth and dissolution in the presence of non-lattice ions which may disturb the movement of lattice cations and anions (Zhang and Nancollas 1998). Whereas a complexation model that couples the effects of Ω with the speciation of the solution and mineral surface successfully describes calcite dissolution rates via defect-assisted etch pit formation in seawater (Naviaux, 2020).

To sum up, even though applying the mechanistic framework of the surface nucleation/dissolution models (i.e., Chernov, 1984; Malkin et al., 1989; Dove et al, 2005) to dissolution rate measurements has proved successful in identifying transitions in mechanisms ($\Omega_{critical}$) (Section 4.2), and the activation energy for crystallization and dissolution (Van Driessche et al., 2010; Naviaux et al., 2019), the linear correlation between step velocity and saturation state may not apply for calcite dissolution in seawater. The possible mechanisms for the nonlinearity are the different attachment and detachment rates ($j^{\pm}$) for the alternating ions in non-Kossel crystals, and the surface complexation processes between the crystal and the ions in seawater.

5. CONCLUSIONS

We report AFM observations of calcite dissolution in seawater for the first time and show no significant difference of etch pit morphology between dissolution in seawater and low ionic strength water – both are rhombic with no significant corner rounding. The ratio of obtuse to acute step velocity is 5–10 in seawater. Solution-based bulk dissolution rate is 2–4 orders of magnitude lower in seawater than in low ionic strength water near equilibrium, but more comparable far from equilibrium. The different responses of dissolution rates to Ω between the two water types are a combined effect of different etch pit densities and step velocities. Even though the dominating dissolution mechanisms and the etch pit densities within the homogeneous etch pit spreading mechanism are the same between seawater and low ionic strength water, the transitions of dissolution mechanisms occur at much higher Ω in seawater, implying a lower surface energy for calcite in seawater than in low ionic strength water. The promotion of etch pit formation in seawater agrees with previously published effect of Mg^{2+} in simple solutions. Although etch pit opening is enhanced, step retreat is inhibited at high and mid-undersaturation states in seawater compared to low ionic strength water, leading to net lower bulk dissolution rates near equilibrium. Step velocities do not depend linearly on Ω in seawater, potentially due to the different attachment and detachment rates for the alternating ions in non-Kossel crystals and the surface complexation processes between the crystal and the ions in seawater.

Declaration of Competing Interest

The authors declare that they have no known competing financial interests or personal relationships that could have appeared to influence the work reported in this paper.

ACKNOWLEDGEMENTS

This work was supported by NSF Ocean Acidification grants (numbers OCE1220600 and OCE1220302), USC Dornsife Doctoral Fellowship, and Grantham Foundation at Caltech. The authors would like to thank four anonymous journal reviewers, as well as the associate editor Dr. Oleg Pokrovsky, for their insightful comments and suggestions that helped to improve this manuscript. We thank Mina Hong, Zibo Li and Liang Zhao for helpful discussions on AFM operations. We also thank Josh West for his suggestions on the manuscript.

APPENDIX A. SUPPLEMENTARY DATA

Supplementary data to this article can be found online at https://doi.org/10.1016/j.gca.2020.05.031.

REFERENCES

Arakaki T. and Mucci A. (1995) A continuous and mechanistic representation of calcite reaction-controlled kinetics in dilute solutions at 25 C and 1 atm total pressure. *Aquat. Geochem.* **1** (1), 105–130.

Arvidson R. S. and Lüttge A. (2010) Mineral dissolution kinetics as a function of distance from equilibrium–New experimental results. *Chem. Geol.* **269**(1–2), 79–88.

Arvidson R. S., Collier M., Davis K. J., Vinson M. D., Amonette J. E. and Lüttge A. (2006) Magnesium inhibition of calcite dissolution kinetics. *Geochimica et Cosmochimica Acta* **70**(3), 583–594.

Arvidson R. S., Ertan I. E., Amonette J. E. and Lüttge A. (2003) Variation in calcite dissolution rates: A fundamental problem? *Geochimica et cosmochimica acta* **67**(9), 1623–1634.

Berger W. H. (1977) Deep-sea carbonate and the deglaciation preservation spike in pteropods and foraminifera. *Nature* **269** (5626), 301–304.

Berner R. A. (1981) Kinetics of weathering and diagenesis. *Rev. Mineral.; (United* **States)**, 8.

Berner R. A. and Morse J. W. (1974) Dissolution kinetics of calcium carbonate in sea water; IV, Theory of calcite dissolution. *Am. J. Sci.* **274**(2), 108–134.

Bisschop J., Dysthe D. K., Putnis C. V. and Jamtveit B. (2006) *In situ* AFM study of the dissolution and recrystallization behaviour of polished and stressed calcite surfaces. *Geochim. Cosmochim. Acta* **70**(7), 1728–1738.

Brady P. V., Krumhansl J. L. and Papenguth H. W. (1996) Surface complexation clues to dolomite growth. *Geochim. Cosmochim. Acta* **60**(4), 727–731.

Brand A. S., Feng P. and Bullard J. W. (2017) Calcite dissolution rate spectra measured by in situ digital holographic microscopy. *Geochim. Cosmochim. Acta* **213**, 317–329.

Brantley S. L., Crane S. R., Crerar D. A., Hellmann R. and Stallard R. (1986) Dissolution at dislocation etch pits in quartz. *Geochimica et Cosmochimica Acta* **50**(10), 2349–2361.

Busenberg E., Plummer L. N. and Mumpton F. A. (1986) A comparative study of the dissolution and crystal growth kinetics of calcite and aragonite. *Studies Diagenesis USGS Bull* **1578**, 139–168.

Chernov A. A. (1984) *Modern Crystallography III: Crystal Growth*. Springer Science & Business Media.

Chernov A. A. (2004) Notes on interface growth kinetics 50 years after Burton, Cabrera and Frank. *J. Cryst. Growth* **264**(4), 499–518.

Chernov A. A., De Yoreo J. J., Rashkovich L. N. and Vekilov P. G. (2004) Step and kink dynamics in inorganic and protein crystallization. *MRS Bull.* **29**(12), 927–934.

Cubillas P., Köhler S., Prieto M., Chaïrat C. and Oelkers E. H. (2005) Experimental determination of the dissolution rates of calcite, aragonite, and bivalves. *Chem. Geol.* **216**(1–2), 59–77.

De Giudici G. (2002) Surface control vs. diffusion control during calcite dissolution: Dependence of step-edge velocity upon solution pH. *Am. Mineral.* **87**(10), 1279–1285.

Dickson A. G. and Millero F. J. (1987) A comparison of the equilibrium constants for the dissociation of carbonic acid in seawater media. *Deep Sea Res. Part A* **34**(10), 1733–1743.

Dickson A. G., Wesolowski D. J., Palmer D. A. and Mesmer R. E. (1990) Dissociation constant of bisulfate ion in aqueous sodium chloride solutions to 250. degree. C. *J. Phys. Chem.* **94**(20), 7978–7985.

Ding H. and Rahman S. R. (2018) Investigation of the Impact of Potential Determining Ions from Surface Complexation Modeling. *Energy Fuels* **32**(9), 9314–9321.

Dong S., Subhas A. V., Rollins N. E., Naviaux J. D., Adkins J. F. and Berelson W. M. (2018) A kinetic pressure effect on calcite dissolution in seawater. *Geochimica et Cosmochimica Acta* **238**, 411–423.

Dove P. M. and Platt F. M. (1996) Compatible real-time rates of mineral dissolution by atomic force microscopy (AFM). *Chem. Geol.* **127**(4), 331–338.

Dove P. M., Han N. and De Yoreo J. J. (2005) Mechanisms of classical crystal growth theory explain quartz and silicate dissolution behavior. *Proc. Natl. Acad. Sci.* **102**(43), 1 5357–15362.

Fenter P., Geissbühler P., DiMasi E., Srajer G., Sorensen L. B. and Sturchio N. C. (2000) Surface speciation of calcite observed in situ by high-resolution X-ray reflectivity. *Geochim. Cosmochim. Acta* **64**(7), 1221–1228.

Fischer C. and Lüttge A. (2007) Converged surface roughness parameters—a new tool to quantify rock surface morphology and reactivity alteration. *Am. J. Sci.* **307**(7), 955–973.

Freij S. J., Putnis A. and Astilleros J. M. (2004) Nanoscale observations of the effect of cobalt on calcite growth and dissolution. *J. Cryst. Growth* **267**(1–2), 288–300.

Gratz A. J., Manne S. and Hansma P. K. (1991) Atomic force microscopy of atomic-scale ledges and etch pits formed during dissolution of quartz. *Science* **251**(4999), 1343–1346.

Gutjahr A., Dabringhaus H. and Lacmann R. (1996) Studies of the growth and dissolution kinetics of the $CaCO_3$ polymorphs calcite and aragonite I. Growth and dissolution rates in water. *J. Cryst. Growth* **158**(3), 296–309.

Harstad A. O. and Stipp S. L. S. (2007) Calcite dissolution: Effects of trace cations naturally present in Iceland spar calcites. *Geochimica et Cosmochimica Acta* **71**(1), 56–70.

Hillner P. E., Gratz A. J., Manne S. and Hansma P. K. (1992) Atomic-scale imaging of calcite growth and dissolution in real time. *Geology* **20**(4), 359–362.

Holdren, Jr, G. R. and Berner R. A. (1979) Mechanism of feldspar weathering—I. Experimental studies. *Geochimica et Cosmochimica Acta* **43**(8), 1161–1171.

Honjo S. and Erez J. (1978) Dissolution rates of calcium carbonate in the deep ocean; an in-situ experiment in the North Atlantic Ocean. *Earth Planet. Sci. Lett.* **40**(2), 287–300.

Keir R. S. (1980) The dissolution kinetics of biogenic calcium carbonates in seawater. *Geochimica et Cosmochimica Acta* **44** (2), 241–252.

Kerisit S. and Parker S. C. (2004) Free energy of adsorption of water and metal ions on the 1014 calcite surface. *J. Am. Chem. Soc.* **126**(32), 10152–10161.

Klasa J., Ruiz-Agudo E., Wang L. J., Putnis C. V., Valsami-Jones E., Menneken M. and Putnis A. (2013) An atomic force microscopy study of the dissolution of calcite in the presence of phosphate ions. *Geochim. Cosmochim. Acta* **117**, 115–128.

Kossel W. (1927) Zur theorie des kristallwachstums. *Nachrichten von der Gesellschaft der Wissenschaften zu Göttingen, Mathematisch-Physikalische Klasse* **1927**, 135–143.

Kowacz M. and Putnis A. (2008) The effect of specific background electrolytes on water structure and solute hydration: Consequences for crystal dissolution and growth. *Geochimica et Cosmochimica Acta* **72**(18), 4476–4487.

Laanait N., Callagon E. B., Zhang Z., Sturchio N. C., Lee S. S. and Fenter P. (2015) X-ray–driven reaction front dynamics at calcite-water interfaces. *Science* **349**(6254), 1330–1334.

Lasaga A. C. and Lüttge A. (2001) Variation of crystal dissolution rate based on a dissolution stepwave model. *Science* **291**(5512), 2400–2404.

Lasaga A. C. (1998) *Kinetic Theory in the Earth Sciences*. Princeton University Press.

Lea A. S., Amonette J. E., Baer D. R., Liang Y. and Colton N. G. (2001) Microscopic effects of carbonate, manganese, and strontium ions on calcite dissolution. *Geochim. Cosmochim. Acta* **65**(3), 369–379.

Liang Y. and Baer D. R. (1997) Anisotropic dissolution at the $CaCO_3$ (10$\bar{1}$4)—water interface. *Surf. Sci.* **373**(2–3), 275–287.

Liang Y., Baer D. R., McCoy J. M., Amonette J. E. and Lafemina J. P. (1996) Dissolution kinetics at the calcite-water interface. *Geochim. Cosmochim. Acta* **60**(23), 4883–4887.

Lippmann F. (1973) *Sedimentary Carbonate Minerals*. Springer-Verlag, Berlin.

Lüttge A. and Arvidson R. S. (2010) Reactions at surfaces: A new approach integrating interferometry and kinetic simulations. *J. Am. Ceram. Soc.* **93**(11), 3519–3530.

Lüttge A., Arvidson R. S. and Fischer C. (2013) A stochastic treatment of crystal dissolution kinetics. *Elements* **9**(3), 183–188.

Lüttge A., Arvidson R. S., Fischer C. and Kurganskaya I. (2019) Kinetic concepts for quantitative prediction of fluid-solid interactions. *Chem. Geol.* **504**, 216–235.

Malkin A. I., Chernov A. A. and Alexeev I. V. (1989) Growth of dipyramidal face of dislocation-free ADP crystals; free energy of steps. *J. Cryst. Growth* **97**(3–4), 765–769.

McCoy J. M. and LaFemina J. P. (1997) Kinetic Monte Carlo investigation of pit formation at the $CaCO_3$ (1014) surface-water interface. *Surf. Sci.* **373**(2–3), 288–299.

Mehrbach C., Culberson C. H., Hawley J. E. and Pytkowicx R. M. (1973) Measurement of the apparent dissociation constants of carbonic acid in seawater at atmospheric pressure1. *Limnol. Oceanogr.* **18**(6), 897–907.

Naviaux J. D. (2020) *Chemical and Physical Mechanisms of Calcite Dissolution in Seawater (Doctoral dissertation*. California Institute of Technology).

Naviaux J. D., Subhas A. V., Rollins N. E., Dong S., Berelson W. M. and Adkins J. F. (2019) Temperature dependence of calcite dissolution kinetics in seawater. *Geochimica et Cosmochimica Acta* **246**, 363–384.

Nehrke G., Reichart G. J., Van Cappellen P., Meile C. and Bijma J. (2007) Dependence of calcite growth rate and Sr partitioning on solution stoichiometry: non-Kossel crystal growth. *Geochimica et Cosmochimica Acta* **71**(9), 2240–2249.

Nielsen L. C., DePaolo D. J. and De Yoreo J. J. (2012) Self-consistent ion-by-ion growth model for kinetic isotopic fractionation during calcite precipitation. *Geochimica et Cosmochimica Acta* **86**, 166–181.

Noiriel C., Oursin M., Saldi G. and Haberthür D. (2018) Direct determination of dissolution rates at crystal surfaces using 3D X-ray microtomography. *ACS Earth Space Chem.* **3**(1), 100–108.

Oelkers E. H., Golubev S. V., Pokrovsky O. S. and Bénézeth P. (2011) Do organic ligands affect calcite dissolution rates? *Geochimica et Cosmochimica Acta* **75**(7), 1799–1813.

Perry, IV, T. D., Duckworth O. W., McNamara C. J., Martin S. T. and Mitchell R. (2004) Effects of the biologically produced polymer alginic acid on macroscopic and microscopic calcite dissolution rates. *Environ. Sci. Technol.* **38**(11), 3040–3046.

Peterson M. N. A. (1966) Calcite: rates of dissolution in a vertical profile in the central Pacific. *Science* **154**(3756), 1542–1544.

Piana S., Jones F. and Gale J. D. (2006) Assisted desolvation as a key kinetic step for crystal growth. *J. Am. Chem. Soc.* **128**(41), 13568–13574.

Plummer L. N., Wigley T. M. L. and Parkhurst D. L. (1978) The kinetics of calcite dissolution in CO_2-water systems at 5 degrees to 60 degrees C and 0.0 to 1.0 atm CO_2. *Am. J. Sci.* **278**(2), 179–216.

Qiu S. R. and Orme C. A. (2008) Dynamics of biomineral formation at the near-molecular level. *Chem. Rev.* **108**(11), 4784–4822.

Rudolph W. W., Michels M. R. and Pye C. C. (2004) Raman, infrared, and ab initio investigation of HPO_4^{2-}(aq). *Science Access* **2**(1), 360–361.

Ruiz-Agudo E., Kowacz M., Putnis C. V. and Putnis A. (2010) The role of background electrolytes on the kinetics and mechanism of calcite dissolution. *Geochimica et cosmochimica acta* **74**(4), 1256–1267.

Ruiz-Agudo E., Putnis C. V., Jiménez-López C. and Rodriguez-Navarro C. (2009) An atomic force microscopy study of calcite dissolution in saline solutions: The role of magnesium ions. *Geochim. Cosmochim. Acta* **73**(11), 3201–3217.

Schott J., Brantley S., Crerar D., Guy C., Borcsik M. and Willaime C. (1989) Dissolution kinetics of strained calcite. *Geochimica et Cosmochimica Acta* **53**(2), 373–382.

Shiraki R., Rock P. A. and Casey W. H. (2000) Dissolution kinetics of calcite in 0.1 M NaCl solution at room temperature: an atomic force microscopic (AFM) study. *Aquat. Geochem.* **6**(1), 87–108.

Sjöberg E. L. (1976) A fundamental equation for calcite dissolution kinetics. *Geochimica et Cosmochimica Acta* **40**(4), 441–447.

Sjöberg E. L. and Rickard D. T. (1984) Temperature dependence of calcite dissolution kinetics between 1 and 62 C at pH 2.7 to 8.4 in aqueous solutions. *Geochim. Cosmochim. Acta* **48**(3), 485–493.

Sjöberg E. L. and Rickard D. T. (1985) The effect of added dissolved calcium on calcite dissolution kinetics in aqueous solutions at 25 C. *Chem. Geol.* **49**(4), 405–413.

Smith M. E., Knauss K. G. and Higgins S. R. (2013) Effects of crystal orientation on the dissolution of calcite by chemical and microscopic analysis. *Chem. Geol.* **360**, 10–21.

Song J., Zeng Y., Wang L., Duan X., Puerto M., Chapman W. G. and Hirasaki G. J. (2017) Surface complexation modeling of calcite zeta potential measurements in brines with mixed potential determining ions (Ca^{2+}, CO_3^{2-}, Mg^{2+}, SO_4^{2-}) for characterizing carbonate wettability. *J. Colloid Interface Sci.* **506**, 169–179.

Stack A. G. and Grantham M. C. (2010) Growth rate of calcite steps as a function of aqueous calcium-to-carbonate ratio: independent attachment and detachment of calcium and carbonate ions. *Cryst. Growth Des.* **10**(3), 1409–1413.

Steefel C. I. and Van Cappellen P. (1990) A new kinetic approach to modeling water-rock interaction: The role of nucleation, precursors, and Ostwald ripening. *Geochimica et Cosmochimica Acta* **54**(10), 2657–2677.

Stipp S. L. S., Eggleston C. M. and Nielsen B. S. (1994) Calcite surface structure observed at microtopographic and molecular scales with atomic force microscopy (AFM). *Geochim. Cosmochim. Acta* **58**(14), 3023–3033.

Stranski I. N. (1928) Zur theorie des kristallwachstums. *Z. Phys. Chem.* **136**(1), 259–278.

Subhas A. V., Adkins J. F., Rollins N. E., Naviaux J., Erez J. and Berelson W. M. (2017) Catalysis and chemical mechanisms of calcite dissolution in seawater. *Proc. Natl. Acad. Sci.* **114**(31), 8175–8180.

Subhas A. V., Rollins N. E., Berelson W. M., Dong S., Erez J. and Adkins J. F. (2015) A novel determination of calcite dissolution kinetics in seawater. *Geochimica et Cosmochimica Acta* **170**, 51–68.

Teng H. H. (2004) Controls by saturation state on etch pit formation during calcite dissolution. *Geochimica et Cosmochimica Acta* **68**(2), 253–262.

Teng H. H. and Dove P. M. (1997) Surface site-specific interactions of aspartate with calcite during dissolution: Implications for biomineralization. *Am. Mineral.* **82**(9–10), 878–887.

Teng H. H., Chen Y. and Pauli E. (2006) Direction specific interactions of 1, 4-dicarboxylic acid with calcite surfaces. *J. Am. Chem. Soc.* **128**(45), 14482–14484.

Uppström Leif R. (1974) The boron/chlorinity ratio of deep-sea water from the Pacific Ocean. *Deep Sea Res. Oceanogr. Abstr.* **21**(2), 161–162. https://doi.org/10.1016/0011-7471(74)90074-6.

Van Driessche A. E., García-Ruiz J. M., Delgado-López J. M. and Sazaki G. (2010) In situ observation of step dynamics on gypsum crystals. *Cryst. Growth Des.* **10**(9), 3909–3916.

Van Heuven, S.M.A.C., Pierrot, D., Rae, J.W.B., Lewis, E., Wallace, D.W.R., 2011. MATLAB program developed for CO2 system calculations. ORNL/CDIAC-105b. Carbon Dioxide Information Analysis Center, Oak Ridge National Laboratory, US Department of Energy, Oak Ridge, Tennessee, 530.

Vinson M. D. and Lüttge A. (2005) Multiple length-scale kinetics: an integrated study of calcite dissolution rates and strontium inhibition. *Am. J. Sci.* **305**(2), 119–146.

Vinson M. D., Arvidson R. S. and Lüttge A. (2007) Kinetic inhibition of calcite (1 0 4) dissolution by aqueous manganese (II). *J. Cryst. Growth* **307**(1), 116–125.

Wolthers M., Nehrke G., Gustafsson J. P. and Van Cappellen P. (2012) Calcite growth kinetics: Modeling the effect of solution stoichiometry. *Geochimica et Cosmochimica Acta* **77**, 121–134.

Xu J., Fan C. and Teng H. H. (2012) Calcite dissolution kinetics in view of Gibbs free energy, dislocation density, and pCO_2. *Chem. Geol.* **322**, 11–18.

Xu M. and Higgins S. R. (2011) Effects of magnesium ions on near-equilibrium calcite dissolution: Step kinetics and morphology. *Geochimica et Cosmochimica Acta* **75**(3), 719–733.

Xu M., Hu X., Knauss K. G. and Higgins S. R. (2010) Dissolution kinetics of calcite at 50–70° C: An atomic force microscopic study under near-equilibrium conditions. *Geochimica et Cosmochimica Acta* **74**(15), 4285–4297.

Yuan K., Starchenko V., Lee S. S., De Andrade V., Gursoy D., Sturchio N. C. and Fenter P. (2019) Mapping three-dimensional dissolution rates of calcite microcrystals: Effects of surface curvature and dissolved metal ions. *ACS Earth Space Chem.* **3**(5), 833–843.

Zhang J. and Nancollas G. H. (1998) Kink Density and Rate of Step Movement during Growth and Dissolution of an AB Crystal in a Nonstoichiometric Solution. *J. Colloid Interface Sci.* **200**(1), 131–145.

Associate editor: Oleg Pokrovsky